Analysis of Photonics-Based RF Beamforming With Large Instantaneous Bandwidth

Xingwei Ye, *Student Member, IEEE*, Dan Zhu, *Member, IEEE*, Yamei Zhang, *Student Member, IEEE*, Simin Li, *Member, IEEE*, and Shilong Pan, *Senior Member, IEEE*

***Abstract*—Since the photonics-based true time delay could significantly broaden the instantaneous bandwidth of a phased antenna array system, solutions utilizing wideband signals could be enabled to considerably enhance the functionality and performance of RF systems. To investigate the features of the wideband beamforming, a comprehensive theoretical model is developed in this paper to analyze the photonics-based broadband beamforming network for uniform linear arrays. In the proposed model, the performance of the beamforming network over the operational frequency band is intuitively depicted through a two-dimensional spatial-temporal frequency response, in which both the spatial frequency (or the corresponding observation angle) and the temporal frequency are adopted as independent variables. In addition, cross correlation of the original signal and the signal that undergoes the beamforming network is calculated to define a wideband pattern and a new figure of merit, so that the waveform-dependent overall response over a large bandwidth can be evaluated. Based on the theoretical model, a time-domain method for pattern measurement is proposed and experimentally demonstrated, which offers the coincident result as the frequency-domain method but is more convenient to be conducted. Numerical results of several typical photonics-based beamforming structures are presented to investigate the impact of nonidealities on the two-dimensional response and the proposed figure of merit.**

***Index Terms*—Array factor, broadband beamforming, correlation reception, optical true time delay.**

I. Introduction

PHASED array antenna (PAA), in which phase shifters are used instead of mechanical components for beam steering, has exhibited its merits as fast beam scanning, flexible beamforming and high reconfigurability [1]. As a key structure for PAA, the beamforming network for providing progressive phases has been a research hotspot [2]–[4]. With the development of broadband RF systems such as electronic warfare systems, multi-protocol wireless communications and high-resolution or multifunctional radars, a beamforming network based on controllable true time delay (TTD) lines is highly desirable to realize squint-free beam steering for signals with large instantaneous bandwidths [5], [6]. Compared to delay devices based on pure electrical techniques, controllable delay lines using photonic or optical techniques could operate with lower loss and broader bandwidth, and could thus become one of the most promising ways to constitute wideband beamforming networks [7], [8]. In the last few decades, substantial progress has been made in the research of optical beamforming networks (OBFNs), in which both the optical delay controlling methods and the structures of optical delay networks are investigated. Many elegant OBFNs have been proposed and demonstrated based on different delay controlling mechanisms including optically switched paths with progressive lengths [9], [10], dispersive elements with multiple lasers or a tunable laser [11]–[17], thermally-tuned ring resonators [18]–[21], etc. Although the broadband feature of OBFNs has been realized, which provides a powerful approach to revolutionizing the PAA systems, the commonly used methods of analyzing and evaluating the performance of an OBFN did not keep pace with the development of the OBFN itself. Usually, the performance of an OBFN is depicted by radiation patterns of the antenna array fed by the OBFN with sinusoidal RF excitation, in which both the measurement in an anechoic chamber or the calculation with the ideal assumption of isotropic antenna elements are acceptable manners in acquiring the patterns. One of the limitations of such methods lies in the single-tone RF excitation because OBFNs are actually designed to be broadband. Such simple excitation could definitely obstruct the research of the distinct feature and the application of large instantaneous bandwidth offered by OBFNs. One possible solution to the problem is to analyze the impulse response of an OBFN and to calculate the integrated antenna pattern (IAP) [22]. The IAP is a wideband pattern that takes the whole signal frequency band into consideration. Based on the viewpoint of total signal energy, the pattern value at each observation angle is defined as the integration of instantaneous power radiated to/from the angle over time. Thus, the overall impact of the OBFN over entire band could be illustrated but detailed response on each frequency is folded. On the contrary, an angle-frequency pattern [23] and a two-dimensional (2D) spatial-temporal frequency response diagram [24], in which the RF temporal frequency is adopted as a new independent variable in addition to the observation angle (or its corresponding spatial frequency), can be applied to describing the change of beamforming response with temporal frequency. Nevertheless,

Manuscript received May 15, 2017; revised August 31, 2017; accepted October 6, 2017. Date of publication October 11, 2017; date of current version November 16, 2017. This work was supported in part by the National Natural Science Foundation of China under Grants 61422108, 61527820, and 61604072, in part by the Natural Science Foundation of Jiangsu Province (BK20160082), and in part by the Fundamental Research Funds for the Central Universities. *(Corresponding author: Shilong Pan.)*

The authors are with the Key Laboratory of Radar Imaging and Microwave Photonics, Ministry of Education, Nanjing University of Aeronautics and Astronautics, Nanjing 211106, China (e-mail: yexw@nuaa.edu.cn; danzhu@nuaa.edu.cn; zhang_ym@nuaa.edu.cn; lisimin@nuaa.edu.cn; pans@ieee.org).

Color versions of one or more of the figures in this paper are available online at http://ieeexplore.ieee.org.

Digital Object Identifier 10.1109/JLT.2017.2762419

the frequency-dependent 2D diagram could not give the overall influence on a specific feeding waveform.

Another limitation in the previous OBFN evaluation methods is the spacing between two adjacent antenna elements in the array. The value of the spacing is commonly taken to be half the wavelength of the RF feeding signal thus the largest grating-lobe-free aperture could be synthesized. Since the operational RF bandwidth of a TTD-based OBFN could achieve multi-octave, the spacing requirement of the lower and the upper frequencies can barely be mediated, indicating that a larger antenna spacing of one or even multiple RF wavelengths could somewhat be inevitable. However, most OBFNs in the literature were just analyzed with half-wavelength antenna spacing, and characteristics in large spacing scenario are expecting for further research.

Recently, we proposed a method of measuring and evaluating the performance of a photonic beamforming-based wideband antenna array [25], [26], in which the frequency-dependent array factor and the feeding waveform-dependent correlation-maximum pattern (CMP) [27], [28] are introduced to depict an OBFN in detail and in general, respectively. The method is not only a combination of the two complementary methods in [22] and [24], but also provides a more sensitive way than the IAP in [22] to evaluate the time-domain distortion because the distortion-induced change in total signal energy may not be as remarkable as the change of correlation peak value that is highly dependent on the signal waveform, as described in [26]. In this paper, we extend our previous work and develop a more comprehensive theoretical model to present the distinct features of an OBFN under the conditions of ultrawide bandwidth and large antenna spacing, which would reveal the intrinsic differences between the TTD-based wideband OBFN and the phase-shifter-based narrowband beamformer. The rest of this paper is organized as follows. Section II describes several general principles and descriptors in the analysis of OBFN, which include the mapping from the optical frequency response to the RF delay response, and the definition of a new figure of merit (FoM) in the OBFN description. The consistency of the 2D spatial-temporal frequency response and the frequency-dependent array factor is also discussed to show that the 2D frequency response in the form of temporal frequency-angle diagram is a better solution to illustrating the OBFN with potential larger antenna spacing. Based on the principles, in Section III, a time-domain method using wideband signal source and oscilloscope is proposed and demonstrated to measure the CMP of a simple wideband beamforming network fed by a linear frequency-modulated (LFM) signal. Numerical results of non-ideal OBFN-induced degradation in the 2D response, the CMP, and the new FoM are provided in Section IV. Section V summarizes this paper and gives some concluding remarks.

II. Theoretical Model

A. Optically Controlling of the TTD of an RF Signal

Fig. 1 depicts a general structure for optically controlling the TTD of an RF signal, in which the RF signal is modulated on an optical carrier, goes through an optical delay element and is

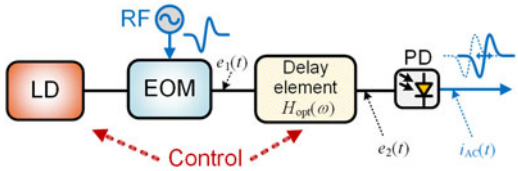

Fig. 1. Schematic diagram of a general optical true time delay (TTD) controller for RF signals. LD: laser diode; EOM: electro-optic modulator; PD: photodetector.

then converted back to the electrical domain in a photodetector (PD). Let the optical carrier be expressed as $\exp(j\omega_c t)$ and the RF signal to be processed be $\cos(\omega_{\mathrm{RF}} t)$. With the assumption of small-signal modulation, i.e., higher order (≥ 2) sidebands can be neglected, the modulated optical field can be expressed as

$$e_1(t) = A_{-1} e^{j(\omega_c - \omega_{\mathrm{RF}})t} + A_0 e^{j\omega_c t} + A_{+1} e^{j(\omega_c + \omega_{\mathrm{RF}})t} \quad (1)$$

in which A_{-1}, A_0, A_{+1} are complex constants determined by the modulation format. For the commonly used intensity modulation using a Mach–Zehnder modulator biased at quadrature point, we have $A_{-1} = A_{+1} = J_1(\gamma)$ and $A_0 = J_0(\gamma)$, where γ is the modulation index and J_n is the nth-order Bessel function of the first kind. If single-sideband (SSB) modulation is applied, A_{-1} or A_{+1} is expected to be zero. The modulated lightwave is then sent to the delay element with an optical frequency response of $H_{\mathrm{opt}}(\omega)$. The output signal can be written as

$$\begin{aligned} e_2(t) = {} & A_{-1} H_{\mathrm{opt}}(\omega_c - \omega_{\mathrm{RF}}) e^{j(\omega_c - \omega_{\mathrm{RF}})t} \\ & + A_0 H_{\mathrm{opt}}(\omega_c) e^{j\omega_c t} + A_{+1} H_{\mathrm{opt}}(\omega_c + \omega_{\mathrm{RF}}) e^{j(\omega_c + \omega_{\mathrm{RF}})t} \end{aligned} \quad (2)$$

After beating in the PD, a RF signal is obtained, given by

$$i_{\mathrm{AC}}(t) \propto \mathrm{Re}\left\{ \begin{aligned} & \exp(j\omega_{\mathrm{RF}} t) \cdot \\ & \left[\begin{aligned} & A_{-1}^* A_0 H_{\mathrm{opt}}^*(\omega_c - \omega_{\mathrm{RF}}) H_{\mathrm{opt}}(\omega_c) \\ & + A_0^* A_{+1} H_{\mathrm{opt}}^*(\omega_c) H_{\mathrm{opt}}(\omega_c + \omega_{\mathrm{RF}}) \end{aligned} \right] \end{aligned} \right\} \quad (3)$$

where the quadratic terms of $A_{\pm 1}$ and the DC terms are ignored, considering the small-signal modulation assumption. Compared with the original RF signal of $\cos(\omega_{\mathrm{RF}} t)$, the controllable phase shift induced by the optical delay is

$$\Delta\varphi(\omega_{\mathrm{RF}}) = \arg\left\{ \begin{aligned} & A_{-1}^* A_0 H_{\mathrm{opt}}^*(\omega_c - \omega_{\mathrm{RF}}) H_{\mathrm{opt}}(\omega_c) \\ & + A_0^* A_{+1} H_{\mathrm{opt}}^*(\omega_c) H_{\mathrm{opt}}(\omega_c + \omega_{\mathrm{RF}}) \end{aligned} \right\} \quad (4)$$

which should fulfill the TTD requirement of

$$\frac{d}{d\omega_{\mathrm{RF}}} \Delta\varphi(\omega_{\mathrm{RF}}) = \text{constant}, \quad \Delta\varphi(0) = 0 \quad (5)$$

As can be seen from (4), the tuning of TTD can be implemented through changing $H_{\mathrm{opt}}(\omega)$. To this end, switched optical paths with progressive lengths and thermally-tuned integrated ring resonators are widely used to construct the optical delay element. Nonlinear effects such as stimulated Brillouin scattering could also help to modify $H_{\mathrm{opt}}(\omega)$ [29], in which the frequency

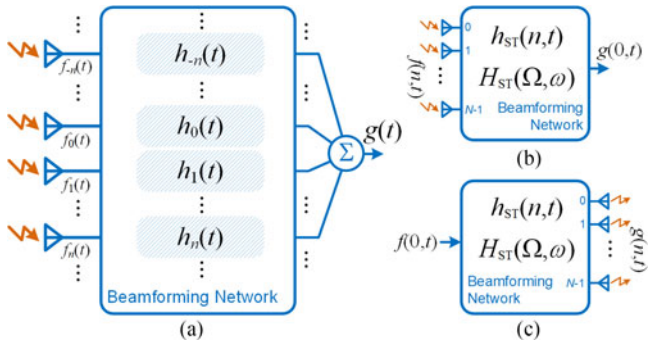

Fig. 2. Beamforming network with the (a) conventional viewpoint in receive mode and the equivalent 2D spatial-temporal filter model in (b) receive and (c) transmit mode.

response in the operational optical band is sensitive to the optical pump power. Especially, if the center frequency of the RF signal to be delayed is much higher than the available optical bandwidth of $H_{\rm opt}(\omega)$, one of the two sidebands could be discarded, which means single sideband modulation should be applied to let A_{-1} or $A_{+1} = 0$. In addition, the carrier could be separated from the modulated sidebands, so that $H_{\rm opt}(\omega_{\rm c})$ and the region around $H_{\rm opt}(\omega_{\rm c}+\omega_{\rm RF})$ or $H_{\rm opt}(\omega_{\rm c}-\omega_{\rm RF})$ could be independently tailored. Another approach to controlling $\Delta\varphi(\omega_{\rm RF})$ is to adjust the carrier frequency $\omega_{\rm c}$ by employing a tunable laser. Thus, a fixed but dispersive element with quadratic phase response can be used for delay controlling. Such quadratic-phase elements include long spools of single-mode fibers, linearly chirped fiber Bragg gratings [11], and photonic crystal fibers [13], which are all harnessed in various TTD-based wideband OBFNs.

B. 2D Spatial-Temporal Frequency Response and Frequency-Dependent Array Factor

Generally, the 2D spatial-temporal frequency response diagram [24] and the frequency-dependent array factor [23], [25], [26] are two major descriptors for wideband beamforming network. Both of the descriptors are functions of two independent variables. One of the variables is the temporal frequency, which could illustrate the change of beamforming response with RF frequency. The other variable, i.e., the spatial frequency in 2D response or the angle in frequency-dependent array factor, is utilized to indicate the dependence of the response on the observation direction. In this part, we will derive the consistency of these two patterns and will show that the angle-frequency pattern, namely the 2D frequency response in the form of temporal frequency-angle diagram, is a better descriptor for depicting the OBFN with potential larger antenna spacing.

Commonly, a beamforming network for a uniform arranged linear array is modeled as a bunch of temporal filters with responses of progressive phase shifts or time delays, as shown in Fig. 2(a). In this structure for receive mode, signals captured by the antenna array are independently processed in their corresponding paths and are then coherently added. The output signal can be found as the summation of temporal convolution on each path

$$g(t) = \sum_n \int_{-\infty}^{+\infty} f_n(\tau) \cdot h_n(t-\tau)\, d\tau \tag{6}$$

where $f_n(t)$ is the signal from the nth antenna, and $h_n(t)$ is the impulse response of the nth path in the beamforming network. To realize the progressive phase shifts or time delays and to simplify the analysis, we assume that $h_{-n}(t)$ and $h_n(t)$ have opposite relative phases or delays with respect to $h_0(t)$.

Consider the case where only N antenna elements with indexes from zero to N-1 are enabled. We have the output as

$$\begin{aligned} g(t) &= \sum_{n=0}^{N-1} \int_{-\infty}^{+\infty} f_n(\tau) \cdot h_n(t-\tau)\, d\tau \\ &= \left\{ \int_{-\infty}^{+\infty} d\tau \left[\sum_{m=-\infty}^{+\infty} f_m(\tau) \cdot h_{m-n}(t-\tau) \right] \right\} \Bigg|_{n=0} \end{aligned} \tag{7}$$

which can be further formatted to a 2D convolution equation

$$g(n,t) = f(n,t) \otimes h_{\rm ST}(n,t)\big|_{n=0} \tag{8}$$

where

$$h_{\rm ST}(n,t) = h_{-n}(t), \quad f(n,t) = f_n(t) \tag{9}$$

Since the spatial index n is listed as a new independent variable, the beamforming network is now a temporal-continuous and spatial-discrete 2D filter with an impulse response of $h_{\rm ST}(n,t)$. To adapt the 2D filter model for the differences in receive and transmit modes, the input $f(n,t)$ and the output $g(n,t)$ of the filter should be clarified. In the receive mode depicted in Fig. 2(b), the N-way input $f(n,t)$ is defined in the range of $0 \le n \le N-1$, and the single superposed signal can be obtained by evaluating the 2D output $g(n,t)$ at a given spatial coordinate $n = 0$. In the transmit mode in Fig. 2(c), the single input takes the only non-zero spatial position of $n = 0$ in $f(n,t)$, and the N-way output signal is $g(n,t)$ where $0 \le n \le N-1$.

As a temporal filter is usually characterized by a temporal frequency response, a beamforming network can also be described using the 2D spatial-temporal frequency response of the corresponding spatial-temporal filter

$$H_{\rm ST}(\Omega,\omega) = \sum_{n=-\infty}^{+\infty} \int_{-\infty}^{+\infty} h_{\rm ST}(n,t)\, e^{-j(\Omega n+\omega t)} dt \tag{10}$$

which is the 2D Fourier transformation of $h_{\rm ST}(n,t)$ with respect to the spatial index n and the time t, and we denote the spatial and the temporal frequency as Ω and ω, respectively. Actually, (10) can be rewritten as

$$H_{\rm ST}(\Omega,\omega) = \sum_{n=-\infty}^{\infty} H_n(\omega)\, e^{j\Omega n} \tag{11}$$

where

$$\begin{aligned} H_n(\omega) &= \int_{-\infty}^{+\infty} h_{\rm ST}(-n,t)\, e^{-j\omega t} dt \\ &= \int_{-\infty}^{+\infty} h_n(t)\, e^{-j\omega t} dt \end{aligned} \tag{12}$$

is the one-dimensional Fourier transformation of $h_n(t)$, namely, the temporal frequency response of the nth path in the beamforming network. Considering the aforementioned clarification in the spatial index n, we can determine the limits of the summation in (11)

$$H_{\mathrm{ST}}(\Omega,\omega)=\sum_{n=0}^{N-1}H_n(\omega)\,e^{j\Omega n} \tag{13}$$

The 2D spatial-temporal frequency response expressed as (13) is the same as the frequency-dependent array factor in [25], [26]

$$H_{\theta T}(\theta,\omega)=\sum_{n=0}^{N-1}H_n(\omega)\cdot\exp\left(jn\frac{\omega d}{c}\sin\theta\right) \tag{14}$$

where θ is the observation angle measured from the broadside direction of the array, d is the uniform spacing between two adjacent elements, and c is the speed of light in vacuum. Comparing (13) and (14), we can simply derive the relationship between the frequency-dependent array factor and the 2D spatial-temporal frequency response in the Ω-ω form as

$$H_{\theta\mathrm{T}}(\theta,\omega)=H_{\mathrm{ST}}(\Omega,\omega)\big|_{\Omega=\mathrm{p.v.}\left(\omega\frac{d}{c}\sin\theta\right)} \tag{15}$$

$$H_{\mathrm{ST}}(\Omega,\omega)=H_{\theta T}(\theta,\omega)\big|_{\theta=\arcsin\left(\frac{c\Omega}{\omega d}\right)},\ |\Omega|\le\frac{\omega d}{c} \tag{16}$$

in which p.v.$(\cdot)$ denotes the principal value wrapped to $(-\pi,+\pi]$. Thus, the intrinsic consistency of the two descriptors is clearly verified, indicating that the frequency-dependent array factor is the 2D spatial-temporal frequency response in the θ-ω form. Note that in (15), the wrapping process implies a possible ambiguity in the mapping from Ω to θ, which could be avoided under the grating-lobe-free condition that the antenna spacing should be no more than half the signal wavelength ($d\le\lambda/2$). However, since the instantaneous bandwidth of a beamforming network is considerably broadened by optical or photonic technologies, such constraint is hardly to be satisfied and should be broken. For instance, consider an ideal 16-way TTD beamforming network working on a large bandwidth of 5–15 GHz. The corresponding spacing between two adjacent antenna elements is 3 cm, which is half the wavelength of a 5-GHz sinusoidal signal, and is 1.5 times of the wavelength of a 15-GHz signal. The Ω-ω and θ-ω 2D frequency responses of this network under a $+60$-degree main lobe configuration are shown in Fig. 3(a) and (b), respectively. In Fig. 3, the two independent variables, i.e., the temporal frequency and the spatial frequency or angle, are denoted as x- and y-axis, respectively. The magnitude of the 2D response is distinguished by different colors. We can see that the main lobe and the grating lobes in the θ-ω diagram are aliased in the Ω-ω diagram, which could lead to ambiguity and could count against the Ω-ω 2D response in characterizing a broadband beamforming system with large antenna spacing. Thus, the 2D response in the θ-ω form is a better descriptor for TTD-based wideband OBFNs and will be adopted in the following part of this paper.

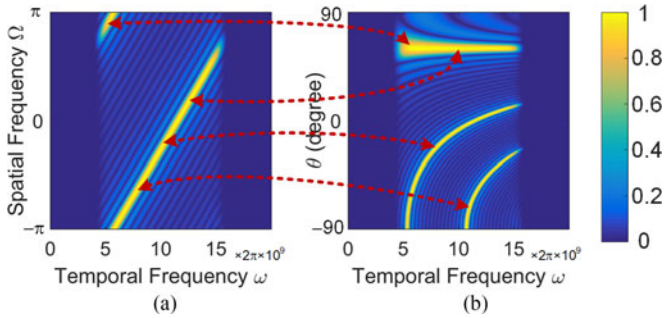

Fig. 3. 2D spatial-temporal frequency responses in (a) the Ω-ω form and (b) the θ-ω form, which characterize a broadband TTD beamforming network for large-spacing antenna array. The red arrows stand for the mapping between the two forms.

C. Correlation-Maximum Pattern and New FoM

The aforementioned 2D spatial-temporal frequency response is intended to illustrate a beamforming network from the detailed viewpoint. To evaluate the overall performance of the network over its entire operational frequency band, we could resort to an algorithm that uses the response data on different temporal frequencies to perform the dimensionality reduction from the 2D response to a simple pattern. Since wideband signals, which put forward the most urgent demands for optical TTD beamforming, are different in waveforms and may suffer from distortion when going through the beamforming network, the representative value for a certain angle should depend on the signal waveforms. Thus, we introduce a reference wideband waveform $s_{\mathrm{ref}}(t)$ as an excitation and assume that the input of a beamforming network in receive mode is

$$f(n,t)=\begin{cases}s_{\mathrm{ref}}\left(t-\dfrac{nd}{c}\sin\theta\right), & 0\le n\le N-1\\ 0, & \text{others}\end{cases} \tag{17}$$

which mimics a source in the far-field region of a d-spacing, N-element antenna array with an incident angle of θ. By sweeping θ, the direction-dependent enhancement/suppression feature of the beamforming network could be acquired. To this end, we firstly use the 2D response or its corresponding impulse response $h_{\mathrm{ST}}(n,t)$ in (8) to calculate the network output $g_\theta(t)$ (or $g_\theta(0,t)$), in which a subscript of θ is added to distinguish the results with different incident angles. Then, cross-correlation of $g_\theta(t)$ and the reference $s_{\mathrm{ref}}(t)$ given by

$$r_\theta(\tau)=\int_{-\infty}^{+\infty}g_\theta(t)\cdot s_{\mathrm{ref}}(t+\tau)\,dt \tag{18}$$

is obtained to show the transmission gain and the distortion of the beamforming network for the θ-direction. The maximum of $r_\theta(t)$ (or its envelop) could be highlighted to compose the CMP

$$CMP(\theta)=\max_\tau\{r_\theta(\tau)\} \tag{19}$$

It was proved that the CMP is more sensitive to the beamforming network-induced signal distortion than the traditional IAP [26], so we believe that the CMP could offer an effective

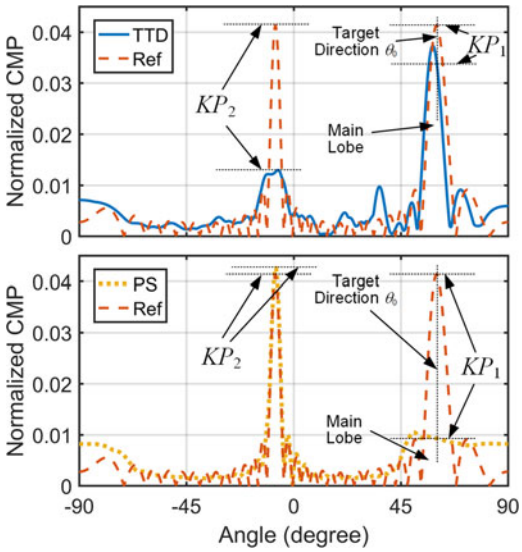

Fig. 4. Typical correlation-maximum patterns (CMPs) with key parameters. KP: key parameter. Solid blue line: a TTD-based OBFN with wideband waveform excitation; dashed red line: a reference ideal phase shifter (PS)-based beamformer with single-tone excitation; dotted yellow line: PS-based beamformer with wideband waveform excitation. The three beamformers share the same center RF frequency, array arrangement, and main lobe direction. A grating lobe near 0° can be observed owing to a large antenna spacing. For PS-based beamformers, beam-squint problem is serious under wideband signal and large main lobe angle, as is shown by the dotted yellow line. Note that the grating lobe does not disperse as the main lobe due to its near-0°-position, which could make the performance of the beamformer even worse.

method of depicting the beamforming network from the macroscopic perspective over the entire band.

The analysis and evaluation of optical TTD beamforming networks also contain the comparison between the performances of different networks. Thus, a FoM should be defined to judge which network could offer superior performance. Here we normalize *CMP*(θ) as

$$\rho(\theta) = \frac{CMP(\theta)}{\int_{-\pi/2}^{+\pi/2} CMP(\varphi)\, d\varphi} \tag{20}$$

Three normalized CMPs are depicted in Fig. 4 as examples, in which the dashed red line stands for a reference ideal phase shifter-based beamformer with single-tone excitation, the dotted yellow line stands for a phase shifter-based beamformer with wideband waveform excitation, and the solid blue line illustrates the pattern of a TTD-based OBFN with wideband waveform excitation. Center RF frequencies, array arrangements, and target directions of the three beamformers are identical. By observing the three typical patterns, we could indicate several key parameters (KPs) that play a major role in beamforming.

KP_1: The value at the target direction θ_0, which represents the domination of the main lobe and prefers a larger value. The deviation of the main lobe could decrease this parameter.

KP_2: The maximum of grating lobes and side lobes, which implies the suppression of all the unwanted spurs and should be smaller.

KP_3: The average of offset angles to the target direction θ_0, which should be smaller and is similar to the concept of variance in probability theory, as given by

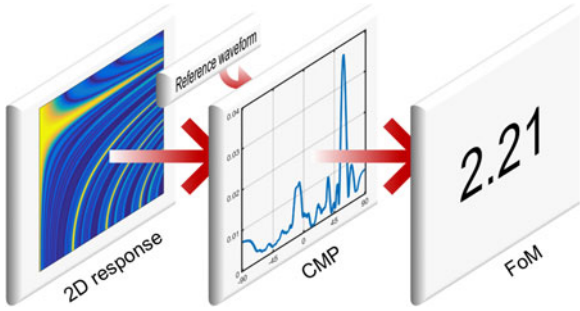

Fig. 5. Three descriptors for the evaluation of TTD-based wideband OBFNs, in which the straight arrows signify the process of dimensionality reduction. FoM: figure of merit.

$$KP_3 = \int_{-\pi/2}^{+\pi/2} (\theta - \theta_0)^2 \rho(\theta)\, d\theta \tag{21}$$

Thus, the relative value of a CMP's KPs with respect to the KPs of the corresponding ideal phase shifter-based beamforming network with single-tone excitation could be used to define the FoM

$$FoM = \frac{KP_1}{KP_1^{\text{ref}}} \cdot \left(\frac{KP_2}{KP_2^{\text{ref}}}\right)^{-1} \cdot \left(\frac{KP_3}{KP_3^{\text{ref}}}\right)^{-1} \tag{22}$$

where KP_x^{ref} are the parameters of the ideal phase shifter-based network with the same center RF frequency, the same array arrangement, and the same target direction. Apparently, a higher FoM corresponds to a better TTD-based wideband OBFN performance.

So far, we have introduced or defined three descriptors for the evaluation of beamforming networks, in which the θ-ω 2D response can be dimensionally reduced to the CMP, and the CMP can be dimensionally reduced to the FoM, as shown in Fig. 5. The three descriptors cover the features of a beamforming network in multiple viewpoints and thus could be a powerful combination to analyze different TTD-based wideband OBFNs.

III. Pattern Measurement in Time Domain

It can be seen from (18) that the network output $g_\theta(t)$, which carries the transmission response of an OBFN, is essential to obtain the CMP and the FoM. Thus, the acquisition of the wideband $g_\theta(t)$ in OBFN experiments deserves further research. In [26], we proposed a method of measuring and calculating $g_\theta(t)$ in the frequency domain, in which the frequency response of each channel in the OBFN, namely $H_n(\omega)$ in (11), is measured with a microwave vector network analyzer and is then multiplied by the spectrum of a reference wideband waveform with a specific delay depending on the antenna index and the incident angle. The inverse Fourier transformation of the superposed results of all the channels could consequently give $g_\theta(t)$.

In fact, since $g_\theta(t)$ is a time-domain signal, the measurement in the time domain, which has already been enabled with the advance in large-instantaneous-bandwidth instruments, could be more straightforward and convenient. The schematic diagram of the time-domain measurement is illustrated in Fig. 6. Signals from an arbitrary waveform generator (Keysight M8195A) are power-amplified and then sent to a horn antenna for radiation.

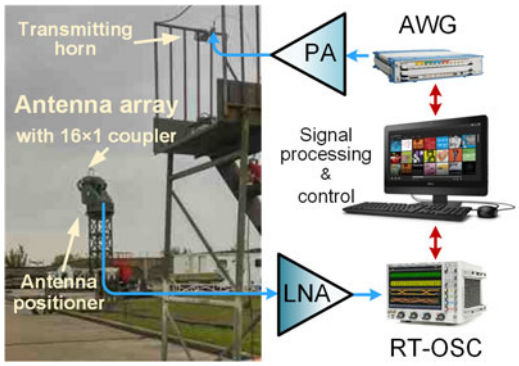

Fig. 6. Schematic diagram of the time-domain measurement in an open area test. AWG: arbitrary waveform generator; PA: power amplifier; LNA: low noise amplifier; RT-OSC: real-time oscilloscope.

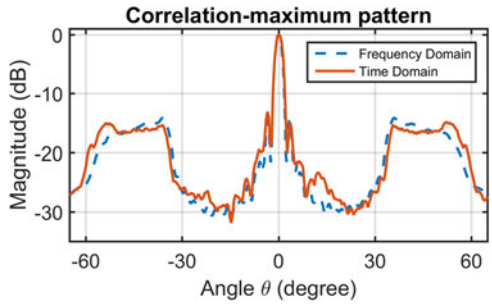

Fig. 7. CMPs of a beamforming system with a wideband linear frequency-modulated signal, which are obtained through the time-domain method and the frequency-domain method, respectively.

The antenna array mounted on a positioner for signal receiving is a 16-element uniform linear array working in the *X*-band. The spacing between two adjacent antenna elements is 4.5 cm, which is as large as 1.5 times of the center RF wavelength. For simplicity and cost consideration, 16 equal-length RF cables are employed instead of microwave photonic links to implement a 0-degree oriented beamforming network. The 16-way signals are coherently added in a 16×1 coupler. After the low noise amplification, the superposed signal, i.e., $g_\theta(t)$, is acquired directly by a real-time oscilloscope (Keysight DSOV334A) and is correlated with the transmitted waveform in a computer. In the experiment, the correlation is performed at each angle in rotation, and the maximum of each correlation result is captured as the value of CMP at the corresponding angle. An 8∼12-GHz wideband LFM signal is transmitted to demonstrate the time-domain measurement, of which the experimental result is depicted in Fig. 7 with the corresponding simulated result using the frequency-domain method. To rule out the unwanted effects around $\pm 90^\circ$ in the experiment, the normalization in Fig. 7 is carried out using the peak value of each trace rather than (20). We can see that two traces agree well with each other, which verifies the feasibility of the measurement in the time domain.

IV. OBFN With Non-idealities: Numerical Examples

In this section, we will use the three descriptors in the preceding part of this paper to study the influence of implementation non-idealities on the OBFN performance with broad instantaneous bandwidth and large antenna spacing. Since the emerging optical delay methods, such as microring resonators [19] and stimulated Brillouin scattering-based slow light [29], could not yet break the tradeoff between the bandwidth and the delay control range, and thus could hardly meet the requirement of the scenario discussed in this paper, here we just select two classical and mature OBFN structures to conduct the analysis.

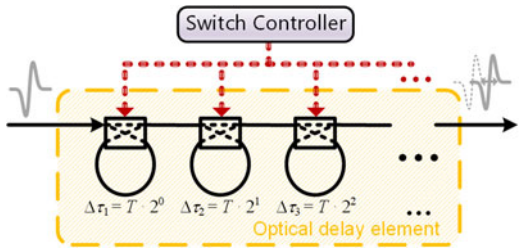

Fig. 8. Schematic diagram of the switch-based optical TTD.

A. Switch-Based TTD OBFN

Switching the length of an optical path is a commonly used method of controlling the optical delay. As is shown in Fig. 8, each switch in the module could control whether an extra length of optical path is involved so that the aggregate delay can be programmed in a large range. Actually, both the discrete optical fiber and the integrated optical waveguide [8] are excellent delay lines that could defeat their electrical counterparts in bandwidth as well as transmission loss. Thus, the switched optical delay line has been a promising solution to constructing OBFNs in not only the traditional discrete form but also the emerging photonic integration. In an optical switch-based TTD beamforming system, each element in the antenna array has a separated optical TTD module, as shown in Fig. 1, in which the kernel optical delay element takes the structure in Fig. 8 and the conventional double sideband (DSB) intensity modulation suffices.

Obviously, the major non-ideality in this kind of OBFN lies in that the switch-based optical TTD could only offer discrete -valued delays, which means the optical frequency response function in (2)–(4) can be expressed as

$$H_{\mathrm{opt,sw}}(\omega) = \exp\left(-j\omega\left[\tau_s/T\right]T\right) \tag{23}$$

where $[\cdot]$ denotes the roundness, τ_s is the target delay for an antenna element, and T is the delay step. For consideration of interchangeability and mass productivity, we assume that switched optical delay lines for antenna elements are identical and share the same delay step. Thus, the performances of OBFNs with different delay setting steps can be calculated with swept main lobe configurations. Due to the symmetry in delay settings, we only conduct the calculation with non-negatively-steered main lobes. A comparison of the results is summarized in Fig. 9(a), in which common parameters are listed in Table I. As expectation, the FoM is generally reduced as the delay step is increased. Note that the fluctuation of FoM with varying main lobe configurations is considerable even if the ideal continuous delay setting is implemented. This is because the FoM defined

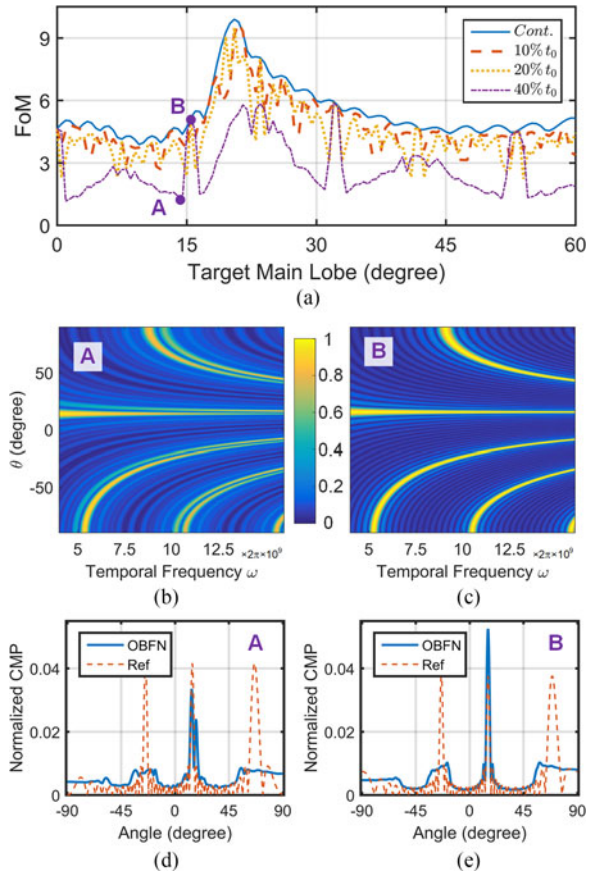

Fig. 9. Performances of the switch-based TTD OBFNs with different delay steps. (a) FoMs under swept main lobe directions, in which t_0 stands for the period of the RF center frequency and is 100 ps here; (b), (c) 2D responses of two representative points in (a); (d), (e) corresponding CMPs and their references with single tone excitation and phase shifters.

TABLE I
PARAMETERS OF THE SWITCH-BASED OBFN IN CALCULATION

Parameter	Value
RF center frequency	10 GHz
Fractional instantaneous bandwidth	0.4
Applied waveform	Linear frequency-modulated
Number of the antennas in the array	16
Antenna spacing	4.5 cm

in (22) is a relative value and is sensitive to the number of grating lobes. When the main lobe is swept from 15° to 20°, a new grating lobe of the center RF frequency around −90° is moving into the visible zone of (−90°∼+90°), which remarkably degrades the CMP of the reference phase shifter-based beamforming network. Meanwhile, since the new grating lobe could also be effectively suppressed by wideband signals [26], key parameters of the CMP in the wideband scenario remain favorable. Thus, the relative performance of the wideband OBFN is greatly boosted. Similarly, the receding of the FoM after the peak near 20° is due to the exiting of the grating lobe around +90°, which gradually recovers the reference CMP and dilutes the relative advantage of the wideband OBFN.

FoM degradation induced by discrete delay settings also changes with the direction of desired main lobe. In Fig. 9(a), points A and B on the trace of FoM with a delay step as large as 40% period of the RF center frequency are two representative cases that could illustrate the worst and the best situations, respectively. The corresponding 2D responses and CMPs are depicted in Fig. 9(b)–(e). For the worst case at point A, the 2D response is somewhat messed with spurs caused by inaccurate discrete delay settings, as in Fig. 9(b). In addition, the main lobe is split into two lobes that dominate at different temporal frequencies, which means further broadening the signal bandwidth would not play a positive role in solving the problem. On the contrary, from Fig. 9(c) we can see that in the best case at point B, the 2D response is quite clear and the main lobe is intact, which enhances the performance of the OBFN to the ideal state. The reason for this enhancement is that the discrete delays provided by switched optical paths are coincidently consistent with the needed progressive time delays. Apparently, a smaller discrete delay step could make the aforementioned consistency more frequent in the sweeping of main lobe direction and could thus boost the overall performance of the switch-based OBFN. Since the shrink of the delay step could bring about a sharp increase in cost due to the rising number of required switches, some continuously controlled devices can be introduced to fill the gaps between discrete delays. A pioneering work on such mixed structures in photonic integration has been reported [18], [21], which could offer a promising solution in the development of OBFN.

The results in Fig. 9 are obtained using ideal switches with infinite extinction ratio, in which a signal could entirely enter the selected path and no leak would be found in the unselected. The ideal lossless delay lines are also employed so that the switching from one path to another would not change the overall link loss. However, in practice, the limited extinction ratio and the inevitable delay line loss could lead to undesired influences, in which the signal after each stage of the switched paths is no longer the correctly delayed one but the sum of a major signal with selected delay and a minor signal with unwanted delay. In addition, notable coupling between the delay and the loss is also introduced. Thus, the requirements on the delay-dependent loss and the extinction ratio in avoiding severe OBFN degradation need to be investigated. Let us involve the loss and the extinction ratio in the simulation and focus on the FoM with the setup of point B in Fig. 9(a). The results are illustrated in a contour map as Fig. 10. We can see that if the loss is lower than 8 dB/ns (0.4 dB/cm for an effective index of 1.5) and the extinction ratio is larger than 26 dB, 90% of the performance of the ideal state with lossless delay lines and ideal switches could be achieved. Such optical waveguides and switches have already been realized in photonic integration [10], [30].

B. Dispersion-Based TTD OBFN

Another kind of TTD OBFN relies on the optical dispersive element, of which the optical frequency response function can be expressed as

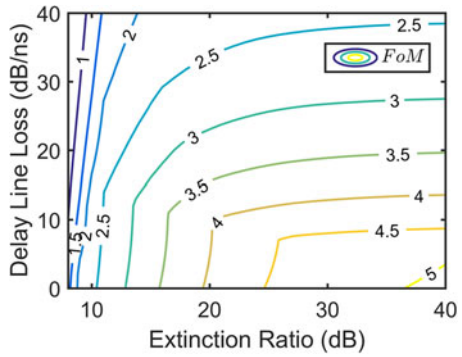

Fig. 10. FoMs of the switch-based TTD OBFN with different extinction ratios of the switches and different delay-dependent losses. Other parameters are the same as point B in Fig. 9(a), in which a 40-ps delay step and a 15.5°-main lobe setting are employed.

$$H_{\mathrm{opt,dp}}(\omega) = \exp\left\{-j\left[\varphi_r + \beta_1(\omega-\omega_r) + \frac{1}{2}\beta_2(\omega-\omega_r)^2\right]\right\} \quad (24)$$

where ω_{r} is a reference optical frequency near the working band, φ_{r} is the phase response at ω_{r}, β_1 and β_2 are the first-and second-order derivatives of the phase response function $\arg[H_{\mathrm{opt,dp}}(\omega)]$ with respect to the temporal frequency. In writing (24), the assumptions of flat amplitude response and negligible higher-order dispersion are taken. According to (4), we can derive the phase shift of a delayed RF signal with a specific frequency ω_{RF} as

$$\Delta\varphi(\omega_{\mathrm{RF}}) = \arg\left\{\begin{array}{l} A_{-1}^* A_0 \exp\left[j\left(-(\beta_1+\beta_2(\omega_c-\omega_r))\omega_{\mathrm{RF}}+\frac{1}{2}\beta_2\omega_{\mathrm{RF}}^2\right)\right] \\ +A_0^* A_{+1}\exp\left[j\left(-(\beta_1+\beta_2(\omega_c-\omega_r))\omega_{\mathrm{RF}}-\frac{1}{2}\beta_2\omega_{\mathrm{RF}}^2\right)\right]\end{array}\right\} \quad (25)$$

As is shown in (25), the parameter of the linear terms in $\Delta\varphi(\omega_{\mathrm{RF}})$ with respect to ω_{RF} is $[\beta_1+\beta_2(\omega_{\mathrm{c}}-\omega_{\mathrm{r}})]$, which means the dispersion induced-delay can be controlled through adjusting either the optical carrier frequency ω_{c} or the dispersion parameter β_2. However, the residual nonlinear terms in $\Delta\varphi(\omega_{\mathrm{RF}})$ would cause signal distortion and RF power fading, and would consequently deteriorate the performance of a dispersion-based OBFN. In fact, such adverse impacts on OBFN and their possible corrections are highly dependent on the structure for producing progressive delays. One of the commonly used dispersion-based OBFN consists of a tunable optical dispersive element and multiple laser sources with progressive but fixed frequencies [16], [17]. Since the dispersive element is shared by all the optical carriers, RF signals for different antenna elements would undergo identical distortion and fading in DSB modulation. Thus, we can utilize SSB modulation to avoid signal impairments and to make the OBFN approximate to the ideal TTD network [17].

Alternatively, one tunable laser source and multiple dispersive elements with fixed progressive dispersion parameters can also be adopted to constitute OBFNs [12], [13], as shown in Fig. 11. In this structure, the main lobe direction is controlled by the laser

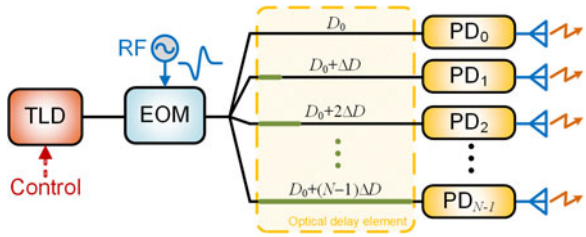

Fig. 11. Structure of the OBFN based on progressive dispersion and tunable laser source. TLS: tunable laser source.

TABLE II
PARAMETERS OF THE DISPERSION-BASED OBFN IN CALCULATION

Parameter	Value
RF center frequency	20 GHz
Fractional instantaneous bandwidth	0.4
Applied waveform	Linear frequency-modulated
Number of the antennas in the array	16
Antenna spacing	2.25 cm
Main lobe direction	Broadside (0°)

frequency rather than the dispersive elements, which implies that more independently-steered RF beams can be realized by simply employing multiple tunable laser sources. However, the progressive dispersion parameters, which impose different RF fading on signals for different antenna elements, could make the non-ideality in OBFN more complicated. With the parameters listed in Table II, the performance of the dispersion-based OBFN in Fig. 11 is numerical simulated. As is shown in Fig. 12(a), a raising step dispersion parameter, ΔD, would severely degrade the OBFN using DSB modulation, and only a moderate improvement could be achieved even if SSB modulation is applied. The corresponding CMPs in Fig. 12(b) and (c) may help to account for the reduction in FoM, in which ΔD is set to 20 ps/nm. In Fig. 12(b), we can see that the main lobe with DSB modulation is split into two parts and the expected peak appears to be a notch. Deviation of the main lobe with SSB modulation from the target direction is also clearly illustrated in Fig. 12(c). Actually, with the optical response function in (24), the two beating terms in (3) have complementary residual quadratic phase terms in addition to the required linear phase terms, which induces the opposite deviation of the main lobe in upper- and lower-SSB modulation, as depicted in Fig. 12(d) and (f). Since DSB modulation is the superposition of the two SSB beatings, the main lobe split in Fig. 12(e) can be understood. It is noteworthy that the main lobe deviation of progressive dispersion-based OBFN with SSB modulation can be precisely predicted, so that a pre-correction in main lobe configuration would effectively improve the beamforming performance, in which the mapping relationship is given by

$$\theta_s' = \left\{\begin{array}{l} \arcsin\left(\sin\theta_s - c\Delta\beta_2\omega_{\mathrm{RF,c}}/(2d)\right), \text{ upper } - \text{ SSB} \\ \arcsin\left(\sin\theta_s + c\Delta\beta_2\omega_{\mathrm{RF,c}}/(2d)\right), \text{ lower } - \text{ SSB}\end{array}\right. \quad (26)$$

where θ_{s}' is the corrected main lobe configuration, θ_{s} is the target direction, $\omega_{\mathrm{RF,c}}$ is the center RF frequency, d is the

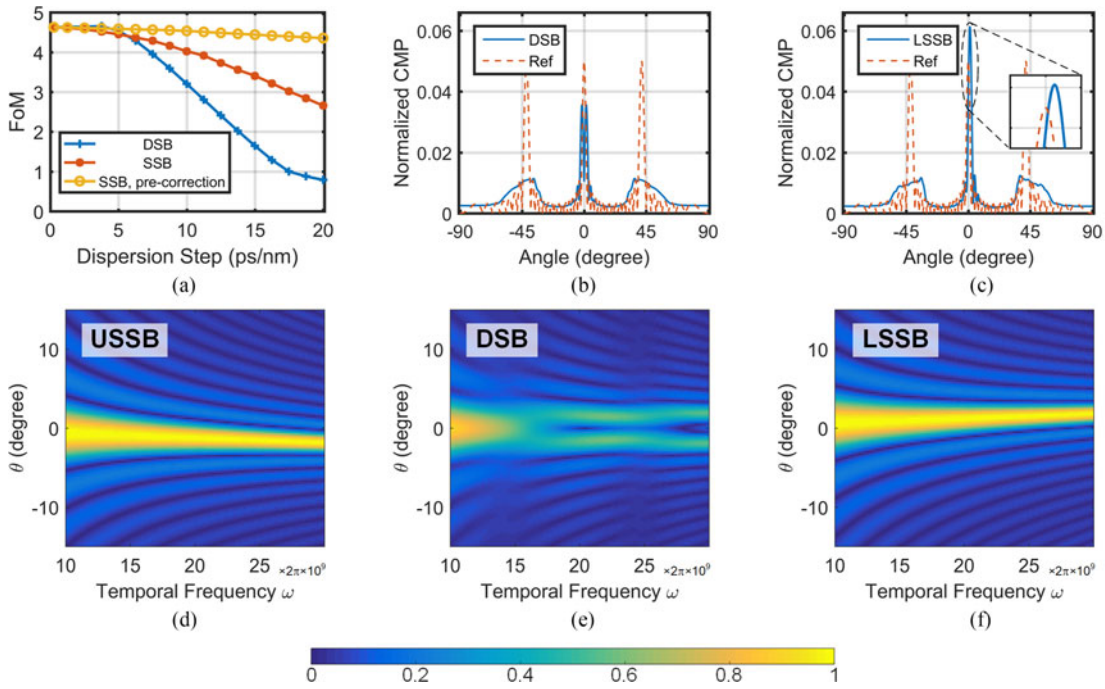

Fig. 12. Performances of the dispersion-based TTD OBFNs with (a) different dispersion steps. (b), (c) Corresponding CMPs and their references with single tone excitation and phase shifters. (d)–(f) 2D responses of the OBFN with different modulation formats. The dispersion step in (b)–(f) is set to the maximum in (a), namely 20 ps/nm. DSB: double sideband; (U/L)SSB: (upper-/lower-) single sideband.

antenna spacing, and $\Delta\beta_2$ is the counterpart of ΔD in temporal frequency form. After the correction, the FoM can be notably boosted, as the dash-dotted line shown in Fig. 12(a). Owing to the fact that (26) is derived at the center RF frequency, a minor distance still exists between the ideal state and the dispersion-based OBFN when wideband waveforms are applied. Of course, this residual error could not cover up the remarkable performance enhancement that is introduced by signals with large instantaneous bandwidths.

V. Discussion and Conclusion

It should be noted that although the analysis of OBFN is mainly conducted by numerical simulation in this paper, the evaluation system with the 2D response, the CMP, and the FoM in Section II can also be used in semi-hardware research, in which multiple microwave photonic links are built without an antenna array entity to concentrate on the OBFN itself and to rule out the impact of antenna elements. To this end, signal delays depending on the incident angle and the arrangement of the antenna elements should be calculated to determine the input of an OBFN, as formulated in (17). The rest of the process is just the same as the one proposed in [26], and the counterpart method in the time domain as described in Section III could also be resorted.

The restriction on the application of the descriptors also deserves to be discussed. In fact, the 2D response in the Ω-ω form requires the most rigorous conditions where the antenna elements should be uniformly arranged and the OBFN should be linear. The 2D response in the θ-ω form could relieve the requirement of uniform arrangement but could not handle the nonlinearity in the RF domain either. Fortunately, the CMP and the FoM based on it could take the nonlinearity into consideration and could properly illustrate its influence. As is discussed in Section III, the output of an OBFN under evaluation can be directly captured in the time domain, so that all the linear and nonlinear effects could be included for further analysis.

In conclusion, we have developed three descriptors to analyze TTD-based OBFN from both the macro- and the micro-prospectives, and have applied them into numerical analyses of two kinds of typical OBFNs. The concepts of 2D filtering and correlation reception are employed in these descriptors and are adapted for meeting the requirements of large antenna spacing and broad instantaneous bandwidth. With the proposed time-domain method in pattern measurement, the analysis and evaluation system in this paper can facilitate the research of photonics-based wideband RF beamforming and can find applications in the design and implementation of future wideband microwave photonic systems.

Acknowledgment

The authors would like to thank Kai Wang, Xiaolin Zhang, Lan Peng and Zhengwu Wei for their help in the antenna array preparation and the open area test.

References

[1] C. A. Balanis, "Arrays: Linear, planar, and circular," in *Antenna Theory: Analysis and Design*, Hoboken, NJ, USA: Wiley, 2005, pp. 283–384.
[2] G. C. Tavik *et al.*, "The advanced multifunction RF concept," *IEEE Trans. Microw. Theory Techn.*, vol. 53, no. 3, pp. 1009–1020, Mar. 2005.
[3] J. Roderick, H. Krishnaswamy, K. Newton, and H. Hashemi, "Silicon-Based ultra-wideband beam-forming," *IEEE J. Solid-State Circuits*, vol. 41, no. 8, pp. 1726–1739, Aug. 2006.

[4] K. Gharibdoust, N. Mousavi, M. Kalantari, M. Moezzi, and A. Medi, "A fully integrated 0.18-μm CMOS transceiver chip for X-Band phased-array systems," *IEEE Trans. Microw. Theory Techn.*, vol. 60, no. 7, pp. 2192–2202, Jul. 2012.
[5] C. Ta-Shun, J. Roderick, and H. Hashemi, "An integrated ultra-wideband timed array receiver in 0.13 μm CMOS using a path-sharing true time delay architecture," *IEEE J. Solid-State Circuits*, vol. 42, no. 12, pp. 2834–2850, Dec. 2007.
[6] C. Ta-Shun and H. Hashemi, "True-time-delay-based multi-beam arrays," *IEEE Trans. Microw. Theory Techn.*, vol. 61, no. 8, pp. 3072–3082, Aug. 2013.
[7] R. Rotman, M. Tur, and L. Yaron, "True time delay in phased arrays," *Proc. IEEE*, vol. 104, no. 3, pp. 504–518, Mar. 2016.
[8] Z. Cao *et al.*, "Advanced integration techniques on broadband millimeter-wave beam steering for 5G wireless networks and beyond," *IEEE J. Quantum Electron.*, vol. 52, no. 1, Jan. 2016, Art. no. 0600620.
[9] D. Dolfi, P. Joffre, J. Antoine, J. P. Huignard, D. Philippet, and P. Granger, "Experimental demonstration of a phased-array antenna optically controlled with phase and time delays," *Appl. Opt.*, vol. 35, pp. 5293–5300, Sep. 1996.
[10] B. Howley, X. Wang, M. Chen, and R. T. Chen, "Reconfigurable delay time polymer planar lightwave circuit for an X-band phased-array antenna demonstration," *J. Lightw. Technol.*, vol. 25, pp. 883–890, Mar. 2007.
[11] J. L. Cruz *et al.*, "Chirped fibre Bragg gratings for phased-array antennas," *Electron. Lett.*, vol. 33, pp. 545–546, Mar. 1997.
[12] P. Wu, S. Tang, and D. E. Raible, "A prototype high-speed optically-steered X-band phased array antenna," *Opt. Express*, vol. 21, pp. 32599–32604, Dec. 2013.
[13] H. Subbaraman, M. Y. Chen, and R. T. Chen, "Photonic crystal fiber-based true-time-delay beamformer for multiple RF beam transmission and reception of an X-band phased-array antenna," *J. Lightw. Technol.*, vol. 26, pp. 2803–2809, Aug. 2008.
[14] X. Ye, F. Zhang, and S. Pan, "Optical true time delay unit for multi-beamforming," *Opt. Express*, vol. 23, pp. 10002–10008, Apr. 2015.
[15] X. Ye, F. Zhang, and S. Pan, "Compact optical true time delay beamformer for a 2D phased array antenna using tunable dispersive elements," *Opt. Lett.*, vol. 41, pp. 3956–3959, Sep. 2016.
[16] B. Ortega, J. Mora, and R. Chulia, "Optical beamformer for 2-D phased array antenna with subarray partitioning capability," *IEEE Photon. J.*, vol. 8, no. 3, Jun. 2016, Art. no. 6600509.
[17] J. Zhang and J. Yao, "Photonic true-time delay beamforming using a switch-controlled wavelength-dependent recirculating loop," *J. Lightw. Technol.*, vol. 34, pp. 3923–3929, Aug. 2016.
[18] M. S. Rasras *et al.*, "Integrated resonance-enhanced variable optical delay lines," *IEEE Photon. Technol. Lett.*, vol. 17, no. 4, pp. 834–836, Apr. 2005.
[19] C. G. H. Roeloffzen *et al.*, "Silicon nitride microwave photonic circuits," *Opt. Express*, vol. 21, pp. 22937–22961, Sep. 2013.
[20] M. Burla *et al.*, "Multiwavelength-integrated optical beamformer based on wavelength division multiplexing for 2-D phased array antennas," *J. Lightw. Technol.*, vol. 32, pp. 3509–3520, Oct. 2014.
[21] T. Tatoli, D. Conteduca, F. Dell'Olio, C. Ciminelli, and M. N. Armenise, "Graphene-based fine-tunable optical delay line for optical beamforming in phased-array antennas," *Appl. Opt.*, vol. 55, pp. 4342–4349, Jun. 2016.
[22] R. Rotman, O. Raz, S. Barzilay, S. R. Rotman, and M. Tur, "Wideband antenna patterns and impulse response of broadband RF phased arrays with RF and photonic beamforming," *IEEE Trans. Antennas Propag.*, vol. 55, no. 1, pp. 36–44, Jan. 2007.
[23] C. Fulton, M. Yeary, D. Thompson, J. Lake, and A. Mitchell, "Digital phased arrays: Challenges and opportunities," *Proc. IEEE*, vol. 104, no. 3, pp. 487–503, Mar. 2016.
[24] C. Wijenayake, A. Madanayake, L. Belostotski, Y. Xu, and L. Bruton, "All-pass filter-based 2-D IIR filter-enhanced beamformers for AESA receivers," *IEEE Trans. Circuits Syst. I, Reg. Papers*, vol. 61, no. 5, pp. 1331–1342, May 2014.
[25] X. Ye, Y. Zhang, and S. Pan, "Performance evaluation of RF beamforming based on a wideband antenna array and photonic true time delay," in *Proc. 2015 Int. Conf. Opt. Commun. Netw.*, 2015, pp. 657–659.
[26] X. Ye, B. Zhang, Y. Zhang, D. Zhu, and S. Pan, "Performance evaluation of optical beamforming-based wideband antenna array," *Chin. Opt. Lett.*, vol. 15, Jan. 2017, Art. no. 010013.
[27] D. Lamensdorf and L. Susman, "Baseband-pulse-antenna techniques," *IEEE Antennas Propag. Mag.*, vol. 36, no. 1, pp. 20–30, Feb. 1994.
[28] J. S. McLean, H. Foltz, and R. Sutton, "Pattern descriptors for UWB antennas," *IEEE Trans. Antennas Propag.*, vol. 53, no. 1, pp. 553–559, Jan. 2005.
[29] I. Aryanfar *et al.*, "Chip-based Brillouin radio frequency photonic phase shifter and wideband time delay," *Opt. Lett.*, vol. 42, pp. 1313–1316, Apr. 2017.
[30] L. Zhuang, D. Marpaung, M. Burla, W. Beeker, A. Leinse, and C. Roeloffzen, "Low-loss, high-index-contrast Si_3N_4/SiO_2 optical waveguides for optical delay lines in microwave photonics signal processing," *Opt. Express*, vol. 19, pp. 23162–23170, Nov. 2011.

Xingwei Ye (S'14) received the B.S. degree in 2014 from Nanjing University of Aeronautics and Astronautics, Nanjing, China, where he is currently working toward the Ph.D. degree at the Key Laboratory of Radar Imaging and Microwave Photonics, Ministry of Education.

His main research interest includes photonic technologies for RF beamforming, synthetic aperture imaging, and direct sampling.

Dan Zhu (M'12) received the B.S. and Ph.D. degrees in electronics engineering from Tsinghua University, Beijing, China, in 2004 and 2009, respectively.

In 2009, she joined the Research Department of Radar Signal Processing, the 14th Research Institute, China Electronics Technology Group Corporation, as a Researcher. In 2011, she joined the Key Laboratory of Radar Imaging and Microwave Photonics, Ministry of Education, Nanjing University of Aeronautics and Astronautics, Nanjing, China, where she is currently an Associate Professor. Her current research interests include photonic microwave and millimeter wave generation, and optical signal processing.

Dr. Zhu is a member of the IEEE Microwave Theory and Techniques Society, the IEEE Photonics Society, and the Optical Society of America.

Yamei Zhang (S'13) received the B.S. degree in 2012 from Nanjing University of Aeronautics and Astronautics, Nanjing, China, where she is currently working toward the Ph.D. degree at the Key Laboratory of Radar Imaging and Microwave Photonics and the Ministry of Education.

Her current research interests include microwave photonic signal generation and processing.

Simin Li (M'17) received the B.S. and Ph.D. degrees from Nanjing University, Nanjing, China, in 2009 and 2014, respectively. In 2014, she joined the Key Laboratory of Radar Imaging and Microwave Photonics, Ministry of Education, Nanjing University of Aeronautics and Astronautics, Nanjing, China, where she is currently a Lecturer. Her current research interests include integrated microwave photonic devices and chips.

Shilong Pan (S'06–M'09–SM'13) received the B.S. and Ph.D. degrees in electronics engineering from Tsinghua University, Beijing, China, in 2004 and 2008, respectively.

From 2008 to 2010, he was a "Vision 2010" Postdoctoral Research Fellow in the Microwave Photonics Research Laboratory, University of Ottawa, Ottawa, ON, Canada. He joined the College of Electronic and Information Engineering, Nanjing University of Aeronautics and Astronautics, China, in 2010, where he is currently a Full Professor and an Executive Director of the Key Laboratory of Radar Imaging and Microwave Photonics, Ministry of Education. His research interest focuses on microwave photonics, which includes optical generation and processing of microwave signals, analog photonic links, photonic microwave measurement, and integrated microwave photonics. He has authored or coauthored more than 300 research papers, including more than 160 papers in peer-reviewed journals, and 140 papers in conference proceedings. He was nominated for the OSA Outstanding Reviewer Award in 2015. He is currently a Topical Editor of Chinese Optics Letters. He is also the Chair of numerous international conferences and workshops, including the TPC Chair of the International Conference on Optical Communications and Networks in 2015, TPC Co-Chair of the IEEE International Topical Meeting on Microwave Photonics in 2017, the TPC Chair of the high-speed and broadband wireless technologies subcommittee of the IEEE Radio Wireless Symposium in 2013, 2014, and 2016, respectively, the TPC Chair of the optical fiber sensors and microwave photonics subcommittee of the OptoElectronics and Communication Conference in 2015, and the Chair of the microwave photonics for broadband measurement workshop of the International Microwave Symposium in 2015.